Uncovering the Lagrangian Skeleton of Turbulence

Manikandan Mathur,[1] George Haller,[1,*] Thomas Peacock,[1] Jori E. Ruppert-Felsot,[2] and Harry L. Swinney[2]

[1]*Department of Mechanical Engineering, MIT, 77 Massachusetts Avenue, Cambridge, Massachusetts 02139, USA*

[2]*Center for Nonlinear Dynamics and Department of Physics, University of Texas at Austin, Austin, Texas 78712, USA*

(Received 22 September 2006; published 4 April 2007)

We present a technique that uncovers the Lagrangian building blocks of turbulence, and apply this technique to a quasi-two-dimensional turbulent flow experiment. Our analysis identifies an intricate network of attracting and repelling material lines. This chaotic tangle, the Lagrangian skeleton of turbulence, shows a level of complexity found previously only in theoretical and numerical examples of strange attractors. We quantify the strength (hyperbolicity) of each material line in the skeleton and demonstrate dramatically different mixing properties in different parts of the tangle.

DOI: 10.1103/PhysRevLett.98.144502 PACS numbers: 47.27.ed, 47.10.Fg, 47.27.De

Turbulent transport underlies a vast range of environmental and engineering phenomena, yet its detailed understanding remains elusive. Coherent structures play a crucial role in turbulent transport, but an objective extraction of such structures from experimental or numerical data has proven to be a challenging task. One difficulty is the lack of an accepted definition for coherence in the Eulerian (laboratory) frame: high or low values of vorticity, pressure, strain, and energy have all been suggested as defining quantities [1,2]. However, different definitions in the Eulerian frame favor different structures partly because of a lack of unambiguous threshold values over which a flow region is to be considered coherent. More alarmingly, Eulerian indicators of coherence are frame dependent [1,3], and hence are often unsuccessful in capturing intrinsic flow properties in unsteady flows.

In contrast, coherent structures in the Lagrangian (particle-based) frame can be defined as distinguished sets of fluid particles. These Lagrangian coherent structures (LCS) have a decisive impact on fluid mixing by their special stability properties [4–7]. For time-periodic laminar flow models, LCS are straightforward to determine using methods developed in studies of chaotic advection [8]; however, it is quite another matter to identify LCS for turbulent flow experiments where stability properties of individual fluid particles are difficult to establish.

Recent experimental work [9] showed that LCS in a time-periodic *laminar* fluid flow mimic the complicated tangles predicted by numerical studies of chaotic advection in time-periodic flow models. In the time-periodic case, velocity measurements for a small number of tracer particles can provide a highly resolved velocity field; the same particles yield more detail about velocity field as time progresses [9]. However, the same approach is inapplicable to turbulent flows for lack of a distinguished period. Further challenges to locating LCS in turbulence are high noise levels and increased spatial complexity, both of which have been absent in LCS studies of time-aperiodic low-Reynolds-number experimental flows [10]. Here we extend LCS detection tools to obtain the analogs of laminar chaotic tangles in a turbulent flow.

Experiment and data processing.—Our experiments are conducted on water in a tank 50 cm high and 40 cm in diameter, rotating at 0.4 Hz [11]. Water is pumped through sources and sinks in the bottom of the tank, thus producing near the bottom of the tank a turbulent three-dimensional (3D) flow with Reynolds number (Re) 6×10^4 and Rossby number (Ro) 20. With increasing height in the tank, the 3D flow evolves into quasi-2D turbulence due to the influence of rotation and the decay of 3D turbulence. This Letter concerns the nearly 2D turbulent flow near the top of the tank, where Re $\approx$ 1000 and Ro $\approx$ 0.3.

Velocity measurements are made on fluid seeded with neutrally buoyant tracer particles illuminated by a horizontal laser light sheet [11]. A camera with resolution 1004×1004 pixels and speed 30 frames/s captures images of the particles. The correlation image velocimetry algorithm [12] is used to determine velocity field snapshots (300 for each run) separated in time by 1/15 s, on a 128×128 spatial grid with 0.3 cm resolution. An analysis of errors is presented in [11].

To postprocess the experimental velocity field, we use cubic interpolation in space and linear interpolation in time to obtain a refined velocity field on a 1500×1500 grid with time step $\Delta t = 0.004$ s. Using refined velocity does not improve the detection of Eulerian coherent structures, but it leads to LCS detection with resolution exceeding that of the raw Eulerian data. By the mathematical properties of hyperbolic sets, any LCS whose length scale is well separated from the refined grid scale is guaranteed to exist in the original flow [7].

Observations.—A snapshot of the vertical vorticity field in a horizontal plane 4 cm below the tank lid is shown in Fig. 1(a); an enlarged image including both vorticity and velocity fields is shown in Fig. 1(b). The flow contains long-lived coherent vortices and jets with a wide range of sizes. Measurements with a vertical laser light sheet reveal that the coherent structures are columnar, extending vertically throughout most of the tank. The quasi-2D flow near the top of the tank is well characterized by the vertical vorticity field [11]. To quantify the two-dimensionality of the flow, we define the integrated Lagrangian divergence,

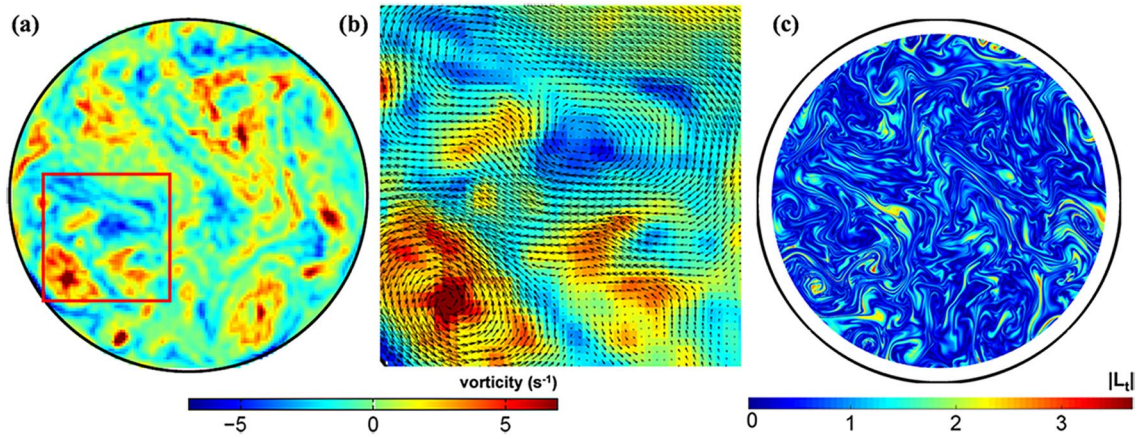

FIG. 1 (color online). (a) A snapshot of the vertical vorticity field in flow in a rapidly rotating tank. The color (gray) scale is saturated to bring out the weaker features. (b) A close-up of the boxed region in (a) with the velocity field indicated by arrows. The largest velocity is 6.5 cm/s and the largest (smallest) value of vorticity is $12.3(-5.8)\ \mathrm{s}^{-1}$. (c) Absolute value of the integrated divergence L_t, which is dimensionless, along particle paths for 8 s in forward time. Regions close to the wall are white because the estimates of the divergence field in those regions are inaccurate.

$L_t(\mathbf{x}_0) = \int_t^{t+T} (\boldsymbol{\nabla} \cdot \mathbf{v})|_{\mathbf{F}_t^s(\mathbf{x}_0)} ds$, where $\mathbf{F}_t^s(\mathbf{x}_0)$ is the position of the fluid particle (whose initial position is $\mathbf{x}_0$ at time t) at time s. The exponential of L_t is the ratio of the deformed area at $t + T$ to the original area of an infinitesimal area element around $\mathbf{x}_0$ at time t [13]. We find that L_t along particle paths (zero for a purely 2D flow) is small throughout most of our flow, taking large values only in small regions [Fig. 1(c)]. Further, as expected for a 2D flow, the spatial mean of the exponential of the integrated divergence is close to unity.

Analysis.—To understand the Lagrangian structure of turbulence, we extend the Lyapunov-exponent-based LCS detection scheme [5] applied previously to laminar-flow experiments with periodic [9] and aperiodic [10] time dependence. Specifically, we solve numerically for particle trajectories $\mathbf{x}(t, \mathbf{x}_0)$, starting from points $\mathbf{x}_0$ on the refined velocity grid at a fixed initial time t_0. By numerical differentiation, we compute the largest singular-value field $\lambda_{\max}(t, t_0, \mathbf{x}_0)$ of the deformation-gradient tensor field $[\partial \mathbf{x}(t, t_0, \mathbf{x}_0)/\partial \mathbf{x}_0]^T [\partial \mathbf{x}(t, t_0, \mathbf{x}_0)/\partial \mathbf{x}_0]$. We then use the direct Lyapunov exponent (DLE) field $\sigma_{t_0}^t(\mathbf{x}_0) = [\ln \lambda_{\max}(t, t_0, \mathbf{x}_0)]/(2(t - t_0))$ plotted over initial positions $\mathbf{x}_0$ to visualize the LCS.

For $t \gg t_0$, repelling LCS at t_0 can be located as local maximizing curves (i.e., *ridges*) of the $\sigma_{t_0}^t(\mathbf{x}_0)$ field [4–7]. Similarly, for $t \ll t_0$, attracting LCS at t_0 can be located as ridges of the $\sigma_{t_0}^t(\mathbf{x}_0)$. For large enough integration times T, sharp evolving ridges of $\sigma_{t_0}^{t_0+T}(\mathbf{x}_0)$ and $\sigma_{t_0}^{t_0-T}(\mathbf{x}_0)$ turn out to be close to evolving material lines, i.e., the fluid flux across them at any time t_0 is negligible [14]. The primary topological features of the LCS extracted from the DLE field is insensitive to the integration time T [5,15]. Accordingly, our analysis of the turbulent data reveals essentially the same topology for T ranging from 1 to 16 s; the ridges are weak at short times and more detailed at long times. We use $T = 8$ s for the results presented here.

A direct Lyapunov exponent field snapshot is shown in Fig. 2. Peaks and valleys on the scale of the grid size are discernible in Fig. 2(a). This noise comes both from measurement uncertainties and from the sensitive nature of

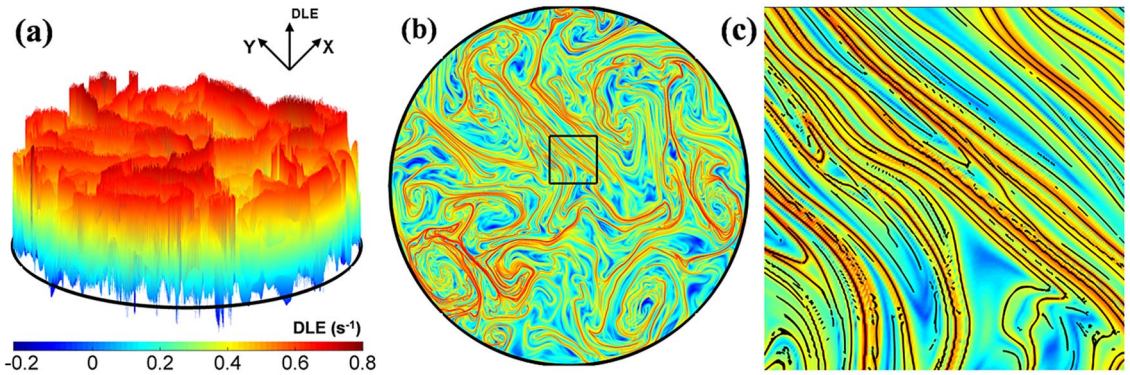

FIG. 2 (color online). (a) A 3D plot of the backward-time DLE field at $t_0 = 9.89$ s (for $T = 8$ s). Note the large amount of noise present in the scalar field. (b) 2D plot of the DLE field shown in (a). (c) Ridges (black curves) of the scalar field in the boxed region in (b), extracted by gradient climbing and filtering.

fluid trajectories in a turbulent flow; consequently, nearby particles end up at very different locations due to inevitable errors in their numerical advection. Corresponding to these different locations, significantly different DLE values arise in our computations, and existing techniques encounter difficulties. We therefore need new computational tools to extract large-scale DLE ridges reliably from our turbulent flow data.

To this end, we note that for any fixed time t_0 and large enough T, a ridge of the DLE field $\sigma_{t_0}^{t_0+T}(\mathbf{x}_0)$ acts as an attractor for the gradient dynamical system

$$d\mathbf{x}_0/ds = \nabla\sigma_{t_0}^{t_0+T}(\mathbf{x}_0), \tag{1}$$

where s denotes the arclength along the gradient lines of $\sigma_{t_0}^{t_0+T}(\mathbf{x}_0)$ and ∇ denotes the spatial gradient with respect to the initial position $\mathbf{x}_0$. We exploit this attracting property in ridge extraction as follows: (i) For any t_0 and large enough T, fix a narrow region D around the ridges where the magnitude of the gradient $\nabla\sigma_{t_0}^{t_0+T}(\mathbf{x}_0)$ exceeds a predefined threshold. This gives a set of points in a close neighborhood of the ridges. (ii) Use these points as initial conditions for computing numerically the solutions $\mathbf{x}_0(s)$ to the gradient system (1). Following these solutions takes us from their initial conditions towards the closest ridge along the local gradient of the DLE field. (iii) For a given initial condition, stop the computation of the corresponding solution $\mathbf{x}_0(s)$ if the following two conditions hold: (a) the Hessian matrix $\nabla^2\sigma_{t_0}^{t_0+T}(\mathbf{x}_0(s))$ has at least one negative eigenvalue (a prerequisite for a point to be on a ridge), and (b) the angle between the eigenvector $\mathbf{e}_{t_0}^{t_0+T}[\mathbf{x}_0(s)]$ corresponding to the smaller-in-norm eigenvalue of the Hessian matrix $\nabla^2\sigma_{t_0}^{t_0+T}(\mathbf{x}_0(s))$ and $\nabla\sigma_{t_0}^{t_0+T}(\mathbf{x}_0(s))$ shows no appreciable change (a sign of closeness to a nearby ridge). For large enough T, the eigenvector $\mathbf{e}_{t_0}^{t_0+T}[\mathbf{x}_0(s)]$ will be approximately tangent to a ridge, and the converged solutions $\mathbf{x}_0(s)$ will approximate ridges accurately. Ridges of the backward-time DLE field extracted in a small region by our algorithm are shown in Fig. 2(c). Similar detail and accuracy have been obtained for the entire spatial domain for a range of values of t_0 and T.

Hyperbolicity criterion.—While hyperbolic material lines create DLE ridges, the converse is *not* true: a DLE ridge may simply indicate a material line of high shear that does not attract or repel nearby particles at an exponential rate [7]. For a DLE ridge to be hyperbolic, it must contain a *hyperbolic core* that plays a role analogous to that of saddle points in steady flows. Namely, a truly repelling DLE ridge will act as a stable manifold for a hyperbolic core, while a truly attracting DLE ridge will act as an unstable manifold for a hyperbolic core.

Previous studies of laminar flows did not differentiate between hyperbolic material lines and lines of high shear. However, the ubiquitous presence of shear in a turbulent flow requires such a differentiation, i.e., identification of hyperbolic cores along DLE ridges. Recent mathematical results [7] enable detection of hyperbolic cores using the rate of strain tensor $\mathbf{S}(\mathbf{x}, t)$, the symmetric part of the velocity gradient field $\nabla\mathbf{v}(\mathbf{x}, t)$. Specifically, if $\mathbf{n}(t_0, \mathbf{x}_0)$ is a unit normal to a forward-time DLE ridge at the point $\mathbf{x}_0$ at time t_0, then $\mathbf{x}_0$ is contained in a hyperbolic core of a repelling material line if the inner product $\nu_{t_0}(\mathbf{x}_0) = \langle \mathbf{n}(t_0, \mathbf{x}_0), \mathbf{S}(t_0, \mathbf{x}_0)\mathbf{n}(t_0, \mathbf{x}_0)\rangle$ is positive. Negative values of the same inner product on a backward-time DLE ridge reveal hyperbolic cores of attracting material lines [7].

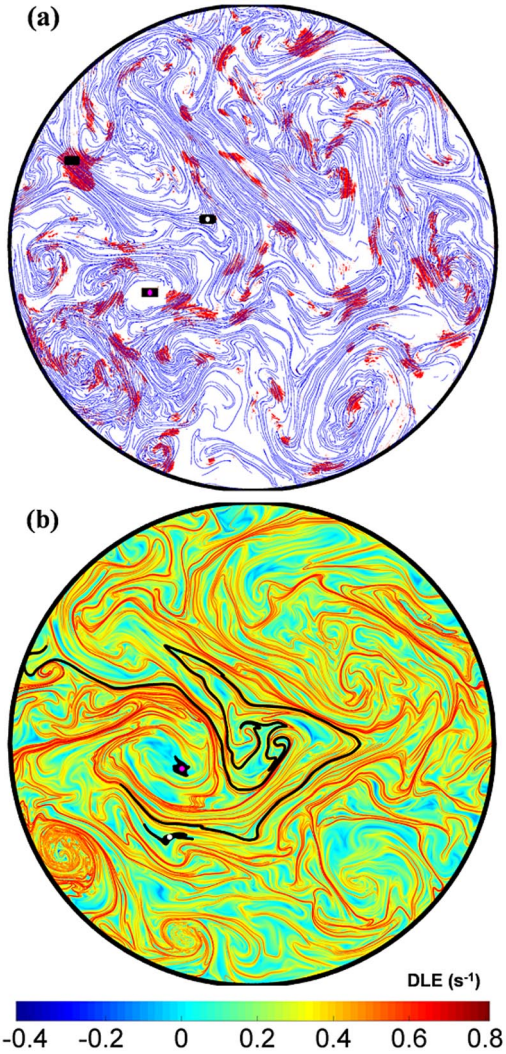

FIG. 3 (color online). (a) Ridges from the backward-time DLE field (at $t_0 = 9.89$ s) are blue (dark gray). Red (gray) spots indicate hyperbolic cores. The boxes indicate the initial locations of three fluid blobs. (b) The three fluid blobs advected with the backward-time DLE field at $t_0 = 16.89$ s. The identifying center dots are not physical.

Figure 3(a), first implementation of the hyperbolicity criterion for a turbulent flow, shows that almost all DLE ridges in our flow field have hyperbolic cores and hence represent truly hyperbolic material lines. The location of hyperbolic cores is verified by advecting a fluid blob starting near a core, e.g., the black blob in Fig. 3, and then comparing the blob's deformation to that of other blobs

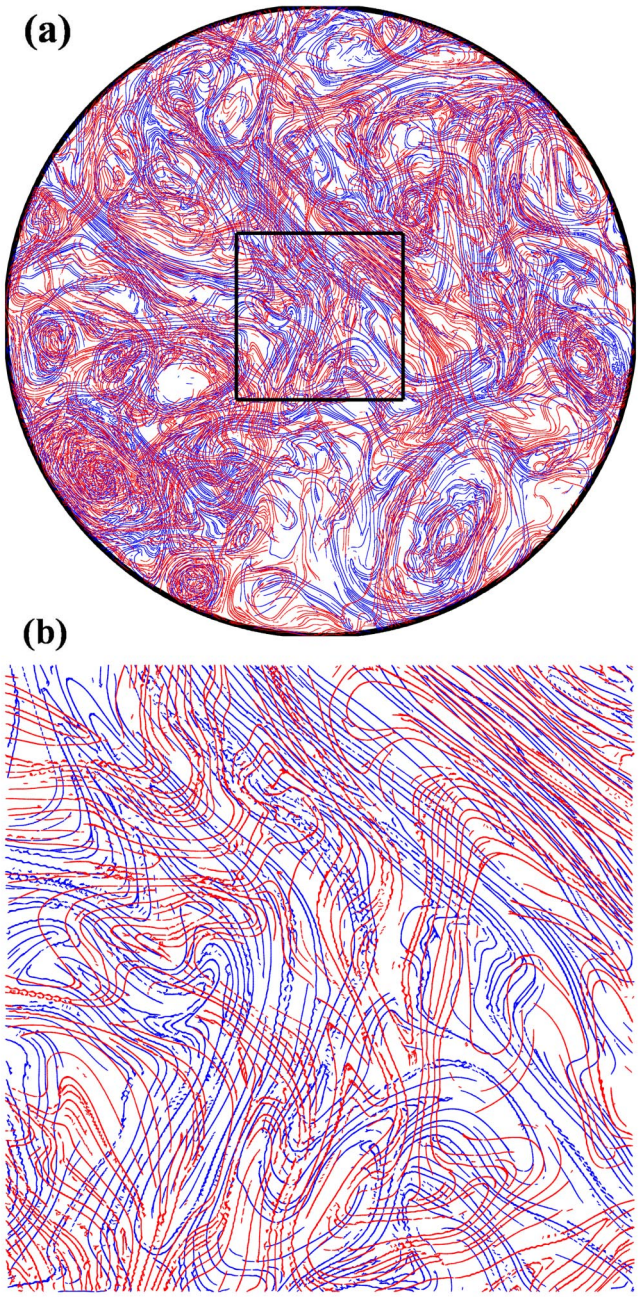

FIG. 4 (color online). (a) Stable (red or gray) and unstable (blue or dark gray) manifolds at $t_0 = 9.89$ s extracted from the experimental flow data as ridges of the forward-time and backward-time DLE fields, respectively. (b) A close-up of the boxed region in (a); the integration time for evaluating the DLE field is 9.8 s.

released away from hyperbolic cores, such as the blob with a white center dot, which was released on an LCS ridge but away from hyperbolic cores, or the blob with a pink (light gray) center dot, which was released away from LCS ridges; there is little stretching of the latter two blobs.

The results in Fig. 3 justify identification of hyperbolic material lines with the set of forward-time and backward-time DLE ridges. Red (gray) ridges in Figs. 4 are stable manifolds for trajectories in the hyperbolic cores, while blue (dark gray) ridges are unstable manifolds for the hyperbolic cores. A fluid particle is subject to attraction to nearby blue (dark gray) curves and simultaneous repulsion by nearby red (gray) curves. The complex tangle formed by these two sets of curves is the underlying cause of turbulent particle motion, the *Lagrangian skeleton of turbulence*. Its complexity is beyond what has been seen for laminar flows. Notably, the skeleton appears to fill the whole flow domain densely with the exception of a single vortical region whose 3-dimensionality cannot be ignored. All hyperbolic cores appear to interact with themselves through homoclinic tangles, as well as with any other core through a chain of intersecting heteroclinic tangles. Such behavior has been observed before only in numerical examples of strange attractors, such as the Lorenz attractor.

Conclusions.—Our analysis reveals an intricate tangle of highly convoluted material lines, the Lagrangian skeleton of turbulence. The complexity of this tangle is unparalleled by material tangles previously reported for laminar flows. The methods developed here extend to 3D flows and are expected to reveal structures of similar complexity. Indeed, recent numerical studies of 3D turbulent channel flows show highly complex LCS structures near hairpin vortices [15].

We thank Jerry Gollub for explanations of his results. The work at MIT was supported by NSF Grant No. DMS-04-04845 and AFOSR Grant AFOSR No. FA 9550-06-0092, and the experiment was conducted in Texas with the support of the Office of Naval Research.

*Corresponding author.
Electronic address: ghaller@mit.edu

[1] J. Jeong and F. Hussain, J. Fluid Mech. **285**, 69 (1995).
[2] J. Davila and J. C. Vassilicos, Phys. Rev. Lett. **91**, 144501 (2003).
[3] G. Haller, J. Fluid Mech. **525**, 1 (2005).
[4] G. Haller and G. Yuan, Physica (Amsterdam) **147D**, 352 (2000).
[5] G. Haller, Physica (Amsterdam) **149D**, 248 (2001).
[6] G. Haller, Phys. Fluids **13**, 3365 (2001).
[7] G. Haller, Phys. Fluids **14**, 1851 (2002).
[8] H. Aref, J. Fluid Mech. **143**, 1 (1984); J. Ottino, Annu. Rev. Fluid Mech. **22**, 207 (1990).
[9] G. A. Voth, G. Haller, and J. P. Gollub, Phys. Rev. Lett. **88**, 254501 (2002).
[10] S. C. Shadden, J. O. Dabiri, and J. E. Marsden, Phys. Fluids **18**, 047105 (2006).
[11] J. E. Ruppert-Felsot, O. Praud, E. Sharon, and H. L. Swinney, Phys. Rev. E **72**, 016311 (2005).
[12] A. Fincham and G. Delerce, Exp. Fluids (Suppl.) **29**, S13 (2000).
[13] V. I. Arnold, *Ordinary Differential Equations* (MIT Press, Cambridge, MA, 1973).
[14] S. C. Shadden, F. Lekien, and J. E. Marsden, Physica (Amsterdam) **212D**, 271 (2005).
[15] M. A. Green, C. W. Rowley, and G. Haller, J. Fluid Mech. **572**, 111 (2007).